

Contents

1	Theoretical Background	1
1.1	Josephson junctions	1
1.1.1	Josephson effect	1
1.1.2	Josephson Junctions in a Magnetic Field	5
1.1.3	RCSJ Model	7
1.2	dc-SQUIDs	11
1.2.1	Zero Voltage State	11
1.2.2	Voltage State	14
1.2.3	Optimal Parameters	16
1.2.4	Noise	17
1.2.5	Parasitic Resonances	18
2	Experimental Setup	23
2.1	Practical dc-SQUIDs	23
2.1.1	Gradiometer	25
2.2	Operation of a dc-SQUID	26
2.2.1	Flux-Locked Loop	26
2.2.2	Two-Stage Configuration	28
2.3	Metallic Magnetic Calorimeters	31
2.3.1	Extrinsic Energy Sensitivity	33
2.4	dc-SQUID Design	35

2.4.1	dc-SQUID with a Two-Turn Input Coil	35
2.4.2	Integrated Two-Stage Chip	35
2.5	Damping Methods	35
2.5.1	Lossy Input Coil	36
2.5.2	Inductive Damping	36
3	Experimental Results	37
3.1	Characteristic dc-SQUID Parameters	37
3.1.1	Input Coil Inductance	37
3.2	Resonance Behavior	37
3.3	Noise Performance	37
3.3.1	Lumped Element Two-Stage Setup	37
3.3.2	Integrated Two-Stage Setup	38
4	Summary	39
	Bibliography	41

1. Theoretical Background

This chapter provides a short introduction into Josephson junctions and their role in dc-SQUIDs (**d**irect **c**urrent **S**uperconducting **Q**Uantum **I**nterference **D**evice), which will be the main focus of this thesis. We start with a brief overview on macroscopic quantum phenomena such as the Josephson effect and explain the general working principle of superconductor-isolator-superconductor (SIS) tunnel contacts, followed by a summary of their basic properties. These tunnel contacts form the theoretical framework to describe the SQUIDs, which are developed in this group and optimized within the scope of this thesis. Lastly, we will take a closer look into their parasitic resonance behavior and investigate chapter different methods to reduce the quality factors. We will closely follow the derivations from the textbooks [Cla04] and [Gro16].

1.1 Josephson junctions

The *Josephson junction* named after Brian D. Josephson consists of two identical superconductors weakly coupled to each other. In the case of the junctions produced in this working group, such coupling is realized through a few nm thin insulating layer between the superconducting electrodes. Consequently, they are also referred to as SIS junctions. The resulting trilayer structure typically consists of Nb/Al-AlO_x/Nb, with niobium being used for the superconductors and the insulating layer being provided by the aluminum oxide. Both superconductors are attributed with a macroscopic quantum mechanical phase θ_1 and θ_2 , respectively. The macroscopic nature of these phases will be explained in subsection 1.1.1. A schematic structure is shown in figure 1.1. By connecting the tunnel junction to a current source they exhibit a non-trivial current-voltage behavior, which will be covered in the following.

1.1.1 Josephson effect

According to the BCS theory developed by Bardeen, Cooper and Schrieffer in 1957 [Bar57], electrons in a superconductor form pairs below a material dependent critical temperature T_c . These composite particles are also referred to as *Cooper pairs* and they represent the superconducting charge carriers with twice the mass and charge of a single electron. Their dissipationless flow causes the current to have zero dc-resistance, which is alongside the Meissner-Ochsenfeld effect [Mei33] the most characteristic feature of a superconductor. The latter describes magnetic field expulsion at the temperature T_c , provided the external magnetic field is smaller than a

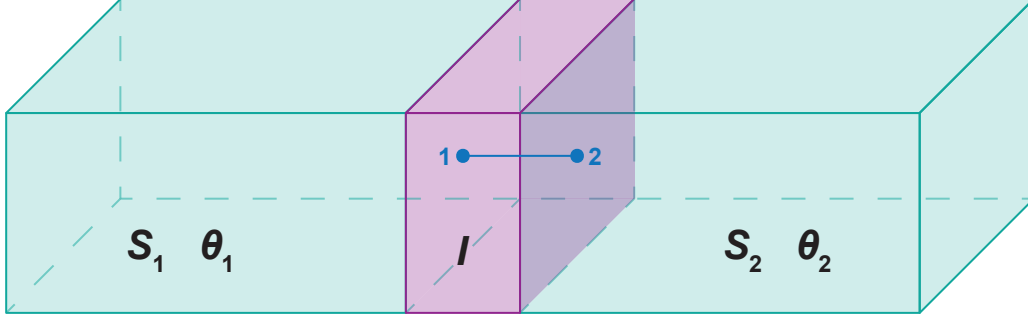


Figure 1.1: Schematic of a Josephson (SIS) junction. Both superconducting electrodes S_1 and S_2 are weakly coupled with each other through a thin tunnel barrier I . θ_1 and θ_2 represent the macroscopic phases of each superconductor.

critical field B_c . Further details on the microscopic theory of superconductivity can be found in [Bar57] and [Gin50].

For temperatures $T < T_c$ ($T_c = 9.3$ K [Ina80]) Cooper pairs are able to tunnel across a Nb/Al-AlO_x/Nb Josephson junction despite the insulating barrier. In fact, their tunneling behavior resembles that of a single electron, which can be motivated by the *Macroscopic Quantum Model* that was formulated by Fritz London in 1953. This model heavily focuses on the quantum mechanical phase θ of a Cooper pair, whose macroscopic nature can be understood by the following arguments. On one hand, the distance between both electrons in a Cooper pair is approximately 10 to 1000 nm which is significantly larger than the spacing between Cooper pairs, resulting in strongly overlapping wave functions. On the other hand, Cooper pairs have to obey Bose-Einstein statistics due to their total spin of 0. Thus, all Cooper pairs share the same ground state, and as a consequence, the energies and temporal evolutions of the phases are equal. These two effects lead to what is known as *phase-lock* [Gro16]. The phases of neighboring pairs synchronize such that this quantum mechanical property now holds on a macroscopic scale. This gives rise to the phase-dependent macroscopic wave function

$$\Psi(\mathbf{r}, t) = \Psi_0(\mathbf{r}, t)e^{i\theta(\mathbf{r}, t)} , \quad (1.1)$$

which describes all charge carriers of a bulk superconductor. Here, the charge carrier density is given by $|\Psi_0(\mathbf{r}, t)|^2 = n_s$. The phase of the Cooper pair ensemble depends on the time t and the position \mathbf{r} . As a result of sharing the same phase, both electrons of a Cooper pair consequently possess the same tunneling probability as an individual electron, enabling the supercurrent. This coherence phenomenon is referred to as the *Josephson effect* [Jos62]. Another significant consequence of the



Figure 1.2: Superconducting ring-shaped cylinder threaded by an external magnetic field. By applying the field at low temperatures, shielding currents arise to expel the field from the superconductor. Upon turning off the external field the shielding currents will remain due to the lack of resistance, causing magnetic flux to be trapped. The dotted blue path C is situated at the center of the cylinder wall, which we assume to be current-free due to the London penetration depth λ_L being much smaller than the thickness of the cylinder wall.

macroscopic quantum model is flux quantization.

This phenomenon can be explained through the capture of an external magnetic flux within a superconducting cylinder (see figure 1.2). The wave function must remain unchanged after circumnavigating the cylinder due to $e^{i\theta} = e^{i\theta+2\pi n}$. As a result, upon integrating along the current-free center of the cylinder wall (path C), the following equation holds for the captured flux [Dea61]

$$\Phi = \frac{h}{q_s}n = \frac{h}{2e}n \equiv \Phi_0 n . \quad (1.2)$$

Here, $n \in \mathbb{Z}$ and $\Phi_0 = 2.07 \times 10^{-15} \text{ T m}^2$ [Tie21] represents the so-called magnetic flux quantum. The captured flux is thus quantized, a consequence solely arising from the macroscopic nature of the phase. This quantity plays a crucial role in the theoretical description of Josephson junctions.

The current and voltage behavior in a SIS junction is described by the *Josephson equations*. Crucial to this description is a critical current I_c that is linearly proportional to the applied current I , which marks the boundary between two operational modes; the zero-voltage state and the voltage state. Additionally, due to the macroscopic nature of the phase, I oscillates with the gauge-invariant phase difference φ , leading to the **first Josephson equation** [Jos65]

$$I_s = I_c \sin(\varphi) . \quad (1.3)$$

The critical current I_c is proportional to the coupling strength κ , which describes the overlap of the wave functions Ψ_1 and Ψ_2 within the insulating layer. The relationship is given by

$$I_c = \frac{4e\kappa V n_s}{\hbar} , \quad (1.4)$$

where V represents the volume of the superconducting electrode and e denotes the elementary charge of an electron. We assume that the Cooper pair density n_s of the two superconductors S_1 and S_2 is identical, meaning $n_{s1} = n_{s2} = n_s$.

The gauge-invariant phase difference refers to the phases θ_1 and θ_2 of the respective electrodes at the boundary of the insulating layer (positions 1 and 2, see figure 1.1). Taking into account possible external electromagnetic fields within the barrier, the general form using the vector potential \mathbf{A} is given by [Gro16]

$$\varphi(\mathbf{r}, t) = \theta_2(\mathbf{r}, t) - \theta_1(\mathbf{r}, t) - \frac{2\pi}{\Phi_0} \int_1^2 \mathbf{A}(\mathbf{r}, t) \cdot d\mathbf{l} . \quad (1.5)$$

Assuming a constant supercurrent density J_s across the junction, taking the time derivative of equation (1.5) yields the **second Josephson equation** [Jos65]

$$\frac{\partial \varphi}{\partial t} = \frac{2\pi}{\Phi_0} V . \quad (1.6)$$

The first of the two above-mentioned operating modes describes the zero-voltage state, i.e. $I < I_c$ (zero-voltage state). Here, the entire injected current is carried by Cooper pairs, so $I = I_s = \text{const.}$ As a result, φ is constant over time, which, according to equation (1.6), leads to $V = 0$. This is known as the *dc Josephson effect*.

For $I > I_c$ however, Cooper pairs begin to break up such that a portion of the current needs to be carried by quasiparticles, which will then lead to a voltage drop V . According to the second Josephson equation, the phase φ becomes time dependent, and after integration one obtains

$$\varphi = \frac{2\pi}{\Phi_0} V t + \varphi_0 = w_J t + \varphi_0 \quad \text{with} \quad w_J = \frac{2\pi}{\Phi_0} V . \quad (1.7)$$

Thus, if we insert equation (1.7) into equation (1.3), we observe that the current I_s oscillates with the *Josephson frequency* $\frac{f_J}{V} = \frac{w_J}{2\pi V} = \frac{1}{\Phi_0} \approx 483.6 \frac{\text{MHz}}{\mu\text{V}}$. Accordingly, this phenomenon is referred to as the *ac Josephson effect*.

1.1.2 Josephson Junctions in a Magnetic Field

To motivate the structure of a dc-SQUID, it is essential to first investigate the current behavior of an extended Josephson junction in the presence of an external magnetic field. So far, all previous formulae apply for point-like junctions, assuming a spatially constant phase difference φ and Josephson current density J_s across the junction area. This is not the case for three-dimensional (extended) junctions with a length L and width W . The *Josephson penetration depth* λ_J is a quantity used to classify an extended junction as short ($W, L \leq \lambda_J$) or long ($W, L \geq \lambda_J$) and is defined as

$$\lambda_J = \sqrt{\frac{\Phi_0}{2\pi\mu_0 J_c t_B}} \quad (1.8)$$

Here, the magnetic thickness is defined as $t_B = d + \lambda_{L,1} + \lambda_{L,2}$, where d is the geometric thickness of the isolator. It describes how far an external magnetic field penetrates



Figure 1.3: Short Josephson junction connected to a current source in the presence of an external B -field in y -direction, parallel to the junction area. Inside the electrodes the magnetic field decays exponentially according to the London penetration depths $\lambda_{L,1}$ and $\lambda_{L,2}$, visually shown by the purple color gradient. The closed contour C is used to derive expressions for the spatially dependent phase difference φ and current density J_s .

both superconducting electrodes if applied parallel to the junction area, as depicted in figure 1.3. The respective London penetration depths are $\lambda_{L,1}$ and $\lambda_{L,2}$ and $J_c = \frac{I_c}{WL}$ is the critical current density. This distinction is needed to determine whether the magnetic self-field generated by the supercurrent is negligible in comparison to the external field (short junctions) or not (long junctions). Within the scope of this thesis, we only use short junctions.

To analyze the current and phase distribution of such a junction we consider the setup shown in figure 1.3. A short junction is connected to a current source and is penetrated by an external B-field in y-direction, parallel to the junction area. Now, obtaining an expression for the phase requires a similar approach as the calculation for the quantized flux, where we assumed that the phase changes by $2\pi n$ around a closed loop. Here, we again integrate over a closed contour C , with the points $P_1 - P_4$ marking the transitions between superconductor and isolator. Using equation 1.5, we find

$$\frac{\partial \varphi}{\partial z} = \frac{2\pi}{\Phi_0} B_y t_B \quad \text{and} \quad \frac{\partial \varphi}{\partial y} = -\frac{2\pi}{\Phi_0} B_z t_B \quad . \quad (1.9)$$

In this experiment, however, the magnetic field points in y-direction only, meaning φ will only vary along the z-axis. Integrating the first expression in equation 1.9 then leads to

$$\varphi(z) = \frac{2\pi}{\Phi_0} B_y t_B z + \varphi_0 \quad . \quad (1.10)$$

Here, the integration constant φ_0 represents the phase difference for the case $z = 0$. Inserting equation 1.10 into the first Josephson equation and using $J_s = \frac{I_s}{WL}$ gives

$$J_s(y, z, t) = J_c(y, z) \sin(kz + \varphi_0) \quad \text{with} \quad k = \frac{2\pi}{\Phi_0} B_y t_B \quad . \quad (1.11)$$

If we now assume the critical current density J_c to be constant across the junction area, we can integrate equation 1.11 to get a flux-dependent maximum Josephson current

$$I_s^m(\Phi) = I_c \left| \frac{\sin\left(\frac{kL}{2}\right)}{\frac{kL}{2}} \right| = I_c \left| \frac{\sin\left(\frac{\pi\Phi}{\Phi_0}\right)}{\frac{\pi\Phi}{\Phi_0}} \right| \quad , \quad (1.12)$$

where $\Phi = B_y t_B L$ is the total flux threading through the junction. This expression describes the so-called Fraunhofer diffraction pattern, shown in figure 1.4. The result resembles the single slit experiment, where the same pattern is found for the light

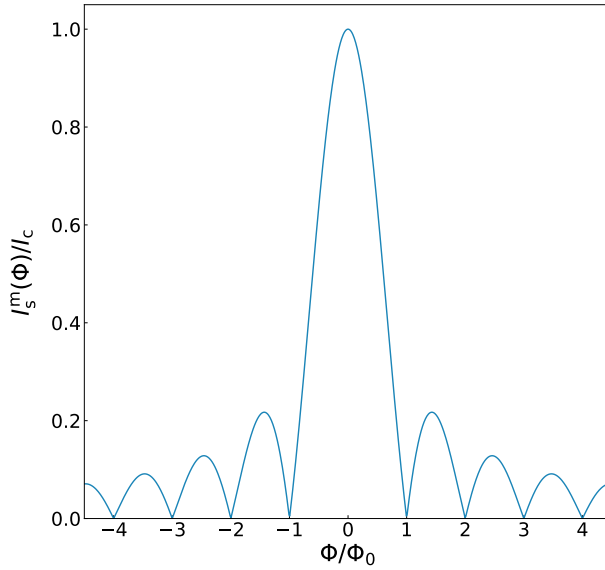


Figure 1.4: Normalized flux-dependent maximum Josephson current $I_s^m(\Phi)$ showing a Fraunhofer pattern. It modulates with the flux quantum Φ_0 , peaking at $\Phi = 0$ with subsequent maxima at $\Phi = \pm(\frac{3}{2} + n)\Phi_0$ with $n \in \mathbb{N}_0$. For $\Phi = \pm(n + 1)\Phi_0$ the total net current is zero.

intensity behind the slit. Here, the analogy works by considering the integral of the critical current density J_c as a transmission function which is constant inside the junction and zero outside.

1.1.3 RCSJ Model

The Fraunhofer pattern describes the flux-dependent current for the case of $I < I_c$, staying in the so-called zero-voltage state. In this regime, only the dc Josephson effect applies as discussed in subsection 1.1.1. Switching to the voltage stage, i.e. $I > I_c$, Cooper pairs start breaking up into quasiparticles if the electric energy eV exceeds the sum of both electrodes' gap energies $\Delta_1(T) + \Delta_2(T)$ [Bar57]. Consequently, at the *gap-voltage*

$$V_g = \frac{\Delta_1(T) + \Delta_2(T)}{e} \quad (1.13)$$

quasiparticles start to cross the tunnel barrier resulting in a steep rise of a resistive normal current I_n . This process also occurs at finite temperatures for $k_B T > \Delta_1(T) + \Delta_2(T)$, leading to a reduction of I_c as well as V_g . Under a dc current source, the condition $I = I_s + I_n$ must be constantly fulfilled. This results in an oscillating normal current and therefore voltage, since I_s oscillates with f_J according to the ac Josephson effect. According to the second Josephson equation (1.6) the oscillating voltage thus causes the term $\frac{d\varphi}{dt}$ to vary sinusoidally, causing both I_s and I_n and

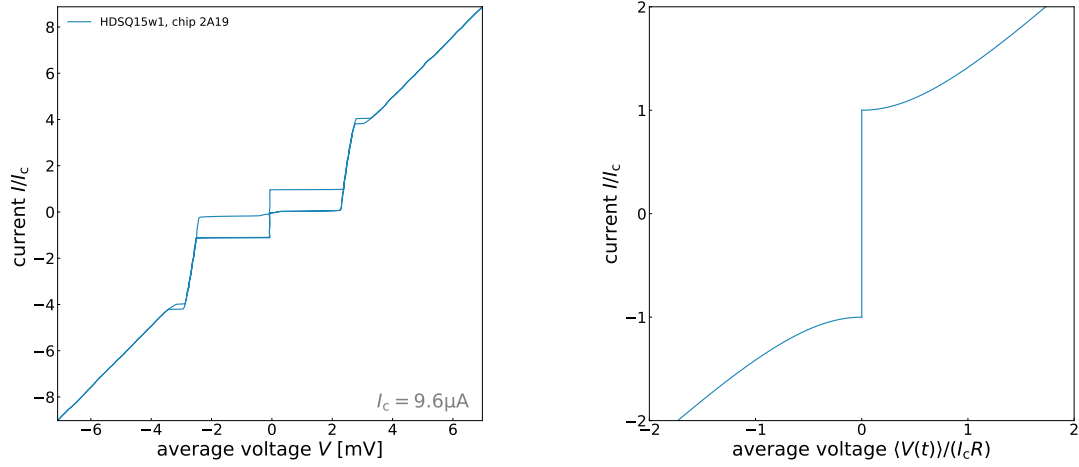


Figure 1.5: Left: Measured IVC of an underdamped junction manufactured in this working group, showing the typical hysteresis. Right: Theoretical IVC of an overdamped junction with a current-voltage shape that is independent of the current sweep direction.

in turn the resulting voltage to oscillate in a complex manner. As a voltage with such a high frequency cannot be measured, only the time-averaged voltage will be considered in the following discussion.

Now, further increasing the energy of the quasiparticles ($T > T_c$ and/or $V > V_g$) leads to a transition into normal-conducting electrons, which exhibit an ohmic dependence. This behavior can be seen in the typical current-voltage-characteristic (IVC) depicted in figure 1.5.

For real junctions, however, one needs to take into account that they are comprised of two electrodes separated by a thin insulating layer, which represent a parallel plate capacitor with the Al-AlO_x layer being the dielectric material. Therefore, a junction capacitance C needs to be taken into account. A displacement current I_d will flow as a consequence, given we are in the voltage state. Lastly, thermal and $1/f$ noise cause a small fluctuating current I_f . All these current channels were defined in the so-called Resistively and Capacitively Shunted Junction (RCSJ) model [McC68], [Ste68], which models the total current of a lumped (0-dimensional) junction to a sufficiently high accuracy. A schematic of an effective circuit diagram is shown in figure 1.6 (left). Combining every current channel leads to the *Basic Junction Equation*, which is defined as [Gro16]

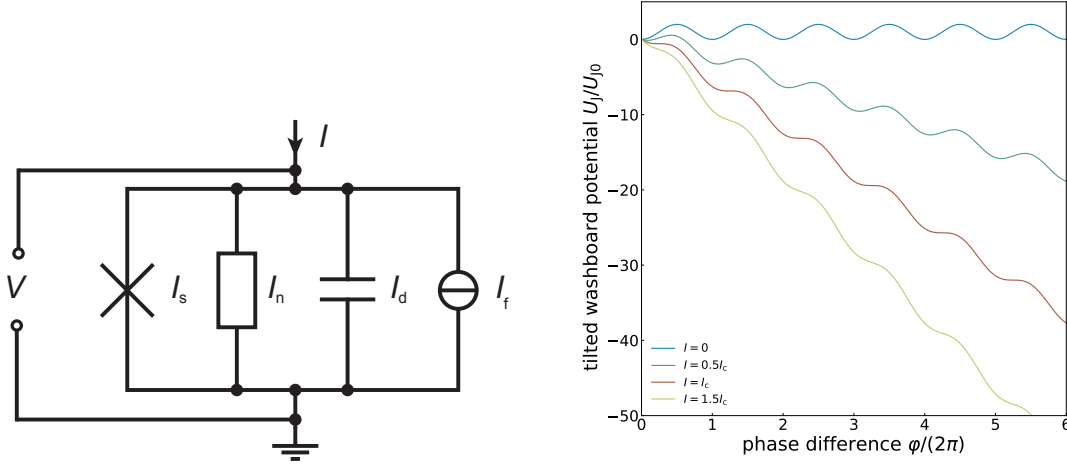


Figure 1.6: Left: Schematic circuit of a lumped Josephson junction with all four current channels connected in parallel, according to the RCSJ model. The junction is represented by the cross symbol on the left, marking the supercurrent I_s . The normal current I_n is realized with a resistance R , while the displacement current I_d and the noise I_f are attributed to a capacitor C and a current source, respectively. Right: Tilted washboard potential for different currents, ranging from 0 to $1.5I_c$. The tilt increases with the injected current I .

$$I = I_s + I_n + I_d + I_f = I_c \sin(\varphi) + \frac{1}{R(V)} \frac{\Phi_0}{2\pi} \frac{d\varphi}{dt} + C \frac{\Phi_0}{2\pi} \frac{d^2\varphi}{dt^2} + I_f \quad (1.14)$$

By defining the Josephson coupling energy $U_{J0} = \frac{\hbar I_c}{2e}$ and the normalized currents $i = \frac{I}{I_c}$ and $i_f(t) = \frac{I_f(t)}{I_c}$, equation 1.14 can be rewritten to

$$\left(\frac{\hbar}{2e}\right)^2 C \frac{d^2\varphi}{dt^2} + \left(\frac{\hbar}{2e}\right)^2 \frac{1}{R(V)} \frac{d\varphi}{dt} + \frac{d}{d\varphi} \{U_{J0} [1 - \cos \varphi - i\varphi + i_f(t)\varphi]\} = 0 \quad (1.15)$$

The expression in the curly brackets represents the potential energy in the system U_J , allowing equation 1.14 to be compared to

$$M \frac{d^2x}{dt^2} + \eta \frac{dx}{dt} + \nabla U = 0 \quad (1.16)$$

which describes a particle with mass M and damping η moving inside the potential U . This mechanical analogue therefore allows us to interpret a *phase particle*, where

it's motion corresponds to a change of the gauge-invariant phase difference φ within a potential U_J [Cla04]. Consequently, it is attributed with a mass $M = \left(\frac{\hbar}{2e}\right)^2 C$ and damping $\eta = \left(\frac{\hbar}{2e}\right)^2 \frac{1}{R(V)}$. Figure 1.6 (right) visualizes how this phase particle behaves for different currents I . Given the shape of $U_J(\varphi)$, the potential is referred to as the *tilted washboard potential*.

For $I = 0$, the phase particle will remain within one of the potential minima. As the current increases, however, the potential starts to tilt such that the depth of the minima reduces until it vanishes for $I = I_c$, thus becoming a saddle point. Up until this point, the phase particle can't overcome the potential barrier to move downward, which agrees with the second Josephson equation as the phase difference φ should remain constant on average for $I < I_c$. Further increasing the current and therefore the tilt of the potential causes the phase particle to fall along the potential, resulting in a voltage drop across the junction ($\frac{\partial \varphi}{\partial t} > 0$).

Reversing the current sweep showcases the importance of the particle's mass M and damping η , as they determine if the return path equals the current shape described above or not. For the case of a small mass (small C) and large damping (small R), the phase particle will, due to a lack of momentum, come to a halt as soon as minima reappear in the washboard potential by reducing the current below I_c . The current path will therefore remain unchanged as I is reduced back to 0, as shown in figure 1.5 (right). Such a junction is consequently called an *overdamped* junction.

The other case describes an *underdamped* junction (figure 1.5 (left)) and involves a large mass (large C) and small damping (large R). This allows the phase particle to continue to move downward as it now carries enough momentum to overcome the arising maxima and minima. The finite voltage drop despite the current being below I_c is displayed as the steep quasiparticle current curve, which ends with a return current I_R that arises with the recapture of the particle in a minimum. This leads to a hysteretic IVC, as depicted in figure 1.5 (left). I_R can be calculated via [Lik86]

$$I_R = \frac{4}{\pi\sqrt{\beta_C}} I_c \quad , \quad (1.17)$$

with β_C being the dimensionless Stewart-McCumber parameter, that is used to quantitatively distinguish between both junction types. It is given by

$$\beta_C = \frac{2\pi}{\Phi_0} I_c R^2 C \quad (1.18)$$

with $\beta_C \gg 1$ corresponding to a strongly underdamped junction, whereas $\beta_C \ll 1$ represents a strongly overdamped junction. The junctions developed and produced within the scope of this thesis aim to be overdamped, which is why we take a closer

look on the time-averaged voltage for $I > I_c$ in the case of $\beta_C \ll 1$. Neglecting the noise in equation 1.15, as well as assuming the resistance to be linear below and above the gap voltage V_g , i.e. $R(V) = R$, the time-averaged voltage can be derived to [Cla04]

$$\langle V(t) \rangle = I_c R \sqrt{\left(\frac{I}{I_c}\right)^2 - 1} \quad \text{for} \quad \frac{I}{I_c} > 1 \quad . \quad (1.19)$$

This equation will be crucial to determine the voltage drop of a dc-SQUID, as its derivation is analogous to that of a single junction, which will be covered in the next section.

1.2 dc-SQUIDS

We have now covered the theoretical framework necessary to understand the working principle of a dc-SQUID, which consists of a superconducting ring intersected by two identical Josephson junctions with critical Josephson currents I_c , as depicted in figure 1.7. Both junctions are shunted with shunt resistors R_s to avoid hysteretic behavior in the respective IVCs. If the loop is then biased with a bias current I_b while being threaded by an external magnetic flux Φ_e , it is possible to convert small flux variations into a measurable voltage change. dc-SQUIDS are therefore used as highly sensitive flux-to-voltage transducers.

1.2.1 Zero Voltage State

In order to fully understand the working principle of a dc-SQUID it is again necessary to first cover the zero voltage stage as we did for a single junction. The parallel connection of the two junctions allows the bias current to split into two supercurrents I_{s1} , I_{s2} with identical critical currents, i.e. $I_{c,1} = I_{c,2} = I_c$. Here we assume $I_b < 2I_c$ to ensure that no voltage drop across both junctions occurs ($V_s = 0$). Applying Kirchhoff's law we then obtain the following expression

$$I_b = I_s = I_c \sin \varphi_1 + I_c \sin \varphi_2 = 2I_c \cos \left(\frac{\varphi_1 - \varphi_2}{2} \right) \sin \left(\frac{\varphi_1 + \varphi_2}{2} \right) \quad . \quad (1.20)$$

In chapter 1.1.2 we concluded that a magnetic flux Φ causes the supercurrent to modulate with Φ_0 . A dc-SQUID can be considered as a single junction with a much larger effective area A_{eff} (loop area), that an external magnetic flux can penetrate. It is therefore reasonable to expect a similar behavior for a dc-SQUID. The same approach as with a single junction is used to determine the flux dependency of the

total supercurrent, where a closed loop integral is performed around the SQUID loop. The calculation leads to the relation [Gro16]

$$\varphi_2 - \varphi_1 = \frac{2\pi\Phi}{\Phi_0} \quad , \quad (1.21)$$

which can be directly inserted into equation 1.20 to obtain

$$I_s = 2I_c \cos\left(\pi \frac{\Phi}{\Phi_0}\right) \sin\left(\varphi_1 + \pi \frac{\Phi}{\Phi_0}\right) \quad . \quad (1.22)$$

In the most general case, however, one needs to take into account the inductance L_s of the SQUID loop and therefore a circulating current $I_{\text{cir}} = \frac{I_{s1} - I_{s2}}{2}$ that induces the additional flux $\Phi_{\text{cir}} = L_s I_{\text{cir}}$. With the external flux Φ_e we can thus write for the total flux

$$\Phi = \Phi_e + \Phi_{\text{cir}} \quad (1.23)$$

$$= \Phi_e - L_s I_c \sin\left(\pi \frac{\Phi}{\Phi_0}\right) \cos\left(\varphi_1 + \pi \frac{\Phi}{\Phi_0}\right) \quad (1.24)$$

$$= \Phi_e - \frac{1}{2}\beta_L \Phi_0 \sin\left(\pi \frac{\Phi}{\Phi_0}\right) \cos\left(\varphi_1 + \pi \frac{\Phi}{\Phi_0}\right) \quad . \quad (1.25)$$

Here, we introduced the dimensionless screening parameter $\beta_L = \frac{2L_s I_c}{\Phi_0}$, which relates the maximum possible flux $\Phi_{\text{cir}}^{\text{max}} = L_s I_{\text{cir}}^{\text{max}} = L_s I_c$ produced by screening currents to $\frac{\Phi_0}{2}$. This quantity describes the influence the screening currents have on the total flux Φ , which in turn affects I_s in equation 1.22. We will now simplify the expression above by considering the limiting case for small currents, i.e. $I_s \ll 2I_c$.

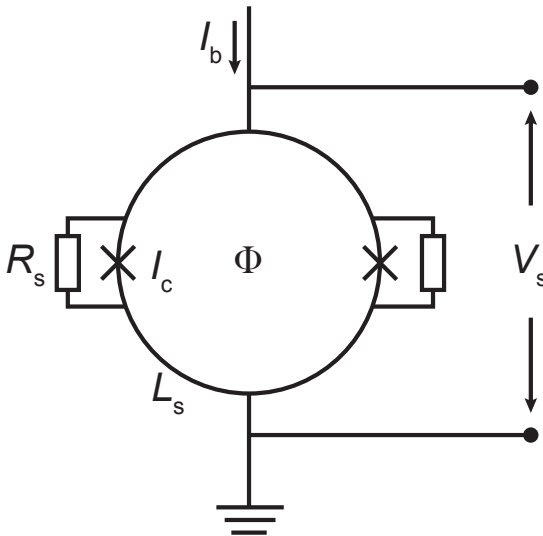


Figure 1.7: Schematic circuit diagram of a shunted dc-SQUID. A superconducting loop with inductance L_s is interrupted by two lumped Josephson junctions such that they form a parallel connection. Operation requires a bias current I_b and an external magnetic flux Φ . To avoid hysteresis effects, a shunt resistance R_s is connected to each junction.

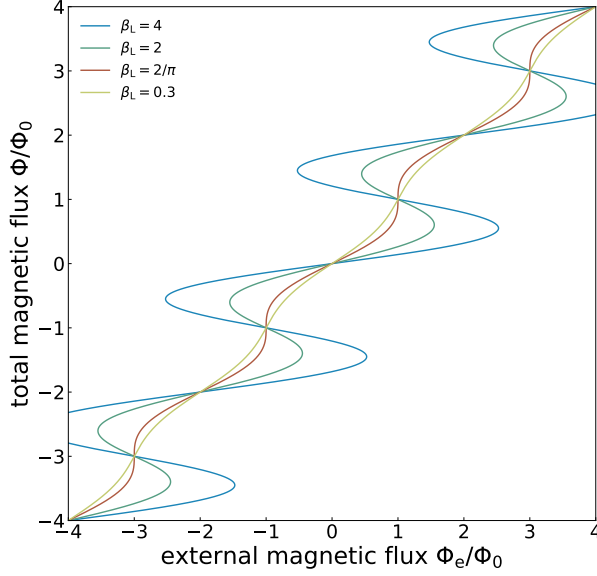


Figure 1.8: Normalized flux Φ modulated by the external flux Φ_e . The amplitude of the modulation depends on the screening parameter β_L , where $\Phi(\Phi_e)$ remains a single-valued function for $\beta_L \leq 2/\pi$.

This condition implies that $\sin \varphi_1 \approx -\sin \varphi_2$ and thus $\varphi_1 \approx -\varphi_2$, leading to a vanishing cosine argument $\varphi_1 + \pi \frac{\Phi}{\Phi_0} \approx 0$. This results in

$$\Phi = \Phi_e - \frac{1}{2}\beta_L \Phi_0 \sin\left(\pi \frac{\Phi}{\Phi_0}\right). \quad (1.26)$$

Figure 1.8 showcases this relation for several values of β_L . High values ($\beta_L > 2/\pi$) correspond to hysteretic characteristics, meaning there can be multiple values of total flux Φ for the same applied flux Φ_e . For practical dc-SQUIDS, it is therefore desirable to avoid this ambiguous behavior. The intersections of each curve represents the case for $\Phi = n\Phi_0$, such that the screening currents vanish and the total flux equals the external flux ($\Phi = \Phi_e$). This is to be expected as the flux in a superconducting ring needs to be quantized (see equation 1.2). Consequently, the SQUID tries to maintain the total flux at integer values of Φ_0 for the limiting case of $\beta_L \gg 1$, where Φ_{cir} dominates over any applied flux. This compensation is visualized by the strong modulation for high β_L in figure 1.8, where a wide range of Φ_e values remain in the proximity of $n\Phi$. The other limiting case, i.e. $\beta_L \ll 1$, allows us to neglect the circulating currents such that we can write $\Phi \approx \Phi_e$. From equation 1.22 we then obtain the maximum possible supercurrent

$$I_s^m(\Phi_e) = 2I_c \left| \cos\left(\pi \frac{\Phi_e}{\Phi_0}\right) \right|. \quad (1.27)$$

The modulation of this current quickly diminishes for increasing β_L , as was derived

in [Cla04] to

$$\frac{\Delta I_s^m(\Phi_e)}{2I_c} \approx 1 - \frac{2\Phi_e}{\Phi_0\beta_L} . \quad (1.28)$$

For the SQUIDs produced within the scope of this thesis, values of $\beta_L \approx 1$ were considered optimal to minimize resonant behavior without reducing the SQUID inductance L_s too much. In subsection 1.2.3 we will discuss how various parameters are chosen to ensure an optimal SQUID performance.

1.2.2 Voltage State

To utilize dc-SQUIDs as sensitive magnetometers, it is necessary to operate them in the voltage state by applying a large enough current bias I_b , such that $I_b > 2I_c$. In the case of negligible screening ($\beta_L \ll 1, \Phi \approx \Phi_e$) and strong damping ($\beta_C \ll 1$), i.e. by choosing a small junction capacitance C and SQUID inductance L_s , it is possible to derive the flux dependency of the resulting voltage drop across the SQUID. Following the RCSJ model, we are only left with the supercurrent I_s and the resistive current I_n , such that by using equation 1.22 we can write for the bias current

$$I_b = 2I_c \cos\left(\pi \frac{\Phi_e}{\Phi_0}\right) \sin\left(\varphi_1 + \pi \frac{\Phi_e}{\Phi_0}\right) + 2\frac{V_s}{R} , \quad (1.29)$$

where we again assumed identical junctions, each shunted by a small shunt resistor $R_s \ll R_n$. Here R_n denotes the normal resistance of a single, unshunted junction. Therefore the total normal resistance R for each parallel connection is approximately $R \approx R_s$. Additionally, we can define a new phase $\varphi = \varphi_1 + \pi \frac{\Phi_e}{\Phi_0}$ and with the maximum supercurrent from equation 1.27 we obtain a current relation that resembles that of a single junction:

$$I_b = I_s^m(\Phi_e) \sin(\varphi) + \frac{2}{R_s} \frac{\Phi_0}{2\pi} \frac{\partial \varphi}{\partial t} . \quad (1.30)$$

This equivalence of a dc-SQUID and a single junction stems from the above-mentioned fact that the SQUID loop represents a single Josephson contact that provides a larger effective area external fields can penetrate. It is therefore possible to derive the voltage drop across the SQUID in the same manner as in subsection 1.1.3. With the critical current $I_s^m(\Phi_e)$ now being flux-dependent with a modulation of Φ_0 , we can

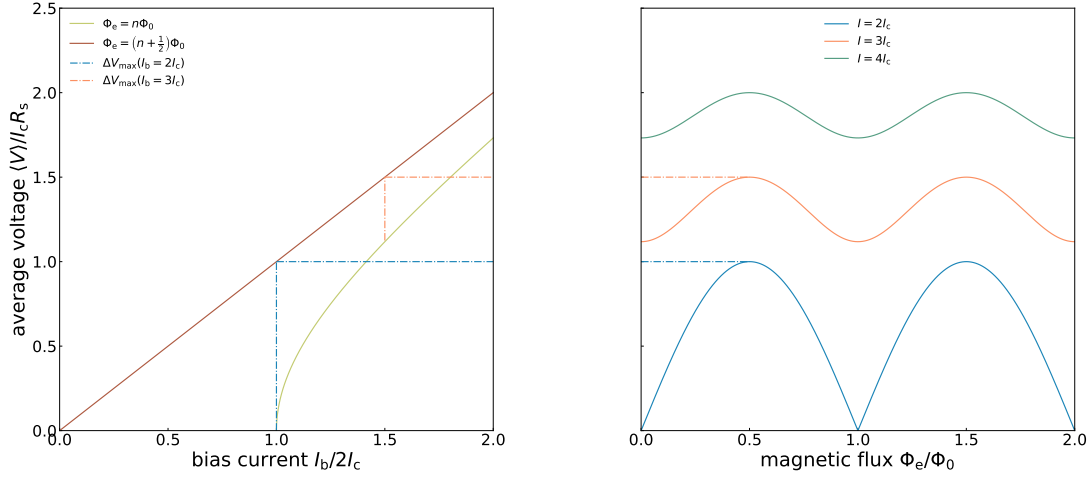


Figure 1.9: Left: IV-characteristics for the total flux $\Phi \approx \Phi_e$ being an integer and half integer number of flux quanta, given that $\beta_C \ll 1$ and $\beta_L \ll 1$. The maximum voltage swing ΔV_{\max} is approximately at $I_b \approx 2I_c$ and corresponds to $I_c R_s$ for a resistively shunted dc-SQUID. Right: The projection of equation 1.31 onto the $V\Phi$ -plane shows the flux dependency of the voltage at the bias current values $I_b = 2I_c$, $I_b = 3I_c$ and $I_b = 4I_c$. The amplitude of the modulation decreases for increasing I_b .

compare to equation 1.19 and obtain for the time averaged voltage [Cla04]

$$\langle V(t) \rangle = \frac{R_s}{2} \sqrt{I_b^2 - I_s^m(\Phi_e)^2} \quad (1.31)$$

$$= I_c R_s \sqrt{\left(\frac{I_b}{2I_c} \right)^2 - \left[\cos \left(\pi \frac{\Phi_e}{\Phi_0} \right) \right]^2}. \quad (1.32)$$

Evidently, both the current and the voltage are flux dependent and are modulated by Φ_0 . Figure 1.9 (left) showcases this behavior by considering the case for the minimum and maximum critical current, i.e. for $\Phi_e = n\Phi_0$ and $\Phi_e = (n + \frac{1}{2})\Phi_0$, with $n \in \mathbb{Z}$. The current-voltage-characteristics at these flux values are particularly interesting, as they can be used to extract crucial SQUID parameters like the voltage swing ΔV_{\max} . This property describes how the voltage varies with the applied flux Φ_e , at a given current I_b . It is maximal at $I_b \approx 2I_c$, as depicted in figure 1.9 (right).

It is, however, important to note that equation 1.31 doesn't hold for practical SQUIDS, as they are typically not fabricated to fulfill the limiting case of $\beta_C \ll 1$ and $\beta_L \ll 1$. The conclusions reached here will nevertheless be applicable to practical SQUIDS, only needing a few adjustments.

1.2.3 Optimal Parameters

Negligible screening is not reasonable, as it would require to choose an extremely small SQUID inductance L_s , which in turn deteriorates the sensitivity for magnetic fields. The main reason to construct a dc-SQUID was to obtain a highly sensitive magnetometer by creating a large area for magnetic fields to thread through. Also, the fabrication process doesn't allow to produce an arbitrarily small junction capacitance C . The parameter β_C will therefore reach a lower limit as well, since also decreasing R_s too much reduces the voltage swing ΔV_{\max} and increases the energy sensitivity $\epsilon(f)$, as we will see in subsection 1.2.4. Now by allowing displacement and fluctuation currents, the current and voltage expressions become analytically unsolvable and therefore have to be solved numerically. In [Tes77] such numerical simulations lead to optimal values of $\beta_C \approx 1$ and $\beta_L \approx 1$ to minimize the energy sensitivity.

To further fine-tune various parameters it is essential to look at how dc-SQUIDs are typically operated to achieve the highest possible flux sensitivity. Here, we distinguish between a current and a voltage bias, where the former was assumed in figure 1.9. Maximizing sensitivity in this mode is done by maintaining the flux through a constant offset at the steepest point in the $V\Phi$ -curve, which is referred to as the working point and corresponds to $\Phi_e = (2n + 1)\frac{\Phi_0}{4}$. This allows for the largest possible voltage change ΔV at a given flux change $\Delta\Phi$. Similarly, at a voltage bias the working point will mark the steepest point in the $I\Phi$ -curve. To quantify this, we introduce the transfer parameters

$$V_\Phi \equiv \left| \left(\frac{\partial V}{\partial \Phi_e} \right) \right| \quad (1.33)$$

$$I_\Phi \equiv \left| \left(\frac{\partial I}{\partial \Phi_e} \right) \right| . \quad (1.34)$$

As mentioned above, at $I_b \approx 2I_c$ (current bias) the amplitude of the voltage modulation is maximal. This needs to be modified for practical SQUIDs, where thermal fluctuations can't be neglected. The resulting thermal current I_{th} causes a rounding of the edge at $I_b = 2I_c$ (figure 1.9 (left)), thereby reducing ΔV_{\max} and V_Φ [Iva68]. To minimize this effect, numerical simulations were made that lead to the condition [Cla88]

$$\frac{I_c}{5} \geq I_{\text{th}} \equiv \frac{2\pi k_B T}{\Phi_0} . \quad (1.35)$$

A lower bound for I_c at $T = 4.2$ K will therefore be approximately 1 μA . This effect

shifts the current $I_{b,\max}$, at which the voltage swing is maximal, according to [Dru96b] by a temperature correction factor leading to

$$I_{b,\max} \approx 2I_c(1 - \sqrt{\Gamma/\pi}) \quad , \quad (1.36)$$

where Γ is the noise parameter defined as $\Gamma = I_{th}/I_c$. Lastly, the thermal current can also be used to set an upper limit to the SQUID inductance. We can define a thermal inductance $L_{th} = \frac{\Phi_0}{2I_{th}}$ for the thermal current inducing half a flux quantum. This should be significantly larger than the SQUID inductance L_s to minimize the impact of these thermal fluctuations. Again, simulations provide a constraint for optimization, giving the relation [Cla88]

$$5L_s \leq L_{th} \equiv \frac{\Phi_0}{2I_{th}} = \frac{\Phi_0^2}{4\pi k_B T} \quad . \quad (1.37)$$

For $T = 4.2\text{ K}$ we would obtain $L_s \leq 1\text{ nH}$, which is typically fulfilled for practical dc-SQUIDS.

1.2.4 Noise

The above-mentioned energy sensitivity, also called spectral noise energy density or energy resolution, is defined as the flux noise per SQUID inductance L_s and is typically expressed through a power spectral density as

$$\epsilon(f) = \frac{S_\Phi(f)}{2L_s} \quad . \quad (1.38)$$

This conveniently allows to compare noise properties from SQUIDS with different loop inductances. The flux noise power spectral density $S_\Phi(f)$ cannot be measured directly and is therefore calculated with the equivalent voltage noise using the transfer coefficient introduced above:

$$S_\Phi(f) = \frac{S_V(f)}{V_\Phi^2} \quad . \quad (1.39)$$

The flux noise in SQUIDS is typically separated into a high frequency constant white noise and a low frequency $1/f$ -noise component [Koc07]. To derive an expression for $S_V(f)$ we consider the white noise regime only, limiting ourselves to higher frequencies to avoid any significant influence of $1/f$ -noise. For this we need to distinguish between two noise currents, one flowing across the SQUID and the other circulating within the SQUID loop. The former sees the total resistance of the SQUID which corresponds

to $\frac{R_s}{2}$ for $I \gg I_{b,\max}$ and to the dynamic resistance $R_{\text{dyn}} = \frac{\partial V}{\partial I}$ for operation at the working point. The circulating current, however, sees two resistances in series, i.e. $2R_s$. By taking into account noise inducing resonances due to the simulated optimal values of $\beta_C \approx 1$ and $\beta_L \approx 1$, both noise currents can be used to obtain the voltage noise given by [Tes77], [Bru82]

$$S_V(f) = \frac{4k_B T}{R_s} \left[2R_{\text{dyn}}^2 + \frac{L_s^2 V_\Phi^2}{2} \right] . \quad (1.40)$$

Here, we used the approximation $V_\Phi \approx \frac{I_c R_s}{\Phi_0/2} \approx \frac{R_s}{L_s}$ for $\beta_L \approx 1$. These calculations also derived the relation $R_{\text{dyn}} \approx \sqrt{2}R_s$, which can be used to rewrite equation 1.40 to

$$S_V(f) = 18k_B T R_s . \quad (1.41)$$

Inserting this into equations 1.39 and 1.38 leads to the expression

$$\epsilon(f) \approx 16k_B T \sqrt{\frac{L_s C}{\beta_C}} \approx 16k_B T \sqrt{L_s C} \quad \text{for } \beta_C \approx 1 . \quad (1.42)$$

For a moderately damped dc-SQUID ($\beta_C \approx 1$) at a temperature $T = 100$ mK and with a suitably small inductance $L_s = 100$ pH we would therefore obtain a theoretical value of $\epsilon \approx 0.32$ h.

Lastly, to get the full picture we will look at the total flux noise spectrum by considering the $1/f$ component. This not entirely understood noise behavior is added to the above derived white noise and dominates the low frequency regime. It is parameterized by a power density at 1 Hz, giving a total noise power density of

$$S_\Phi(f) = S_{\Phi,w} + \frac{S_{\Phi,1/f}(1 \text{ Hz})}{f^\alpha} , \quad (1.43)$$

with $S_{\Phi,w}$ being the white noise component and α ranging between 0.5 and 1 [Dru11], which can be determined through experiment.

1.2.5 Parasitic Resonances

We have seen that optimizing dc-SQUID properties requires careful fine-tuning of various parameters to ensure high sensitivity and low noise at the same time. Another constraint in this regard involves the presence of resonances in the system that we need to take into account. As discussed in subsection 1.1.3, a Josephson contact



Figure 1.10: Measured IV-characteristic of a dc-SQUID developed within the scope of this thesis. The first current step at $V_s \approx 40 \mu\text{V}$ corresponds to the fundamental SQUID resonance for $L_s = 119 \text{ pH}$ and $C = 0.95 \text{ pF}$.

represents a parallel plate capacitor with capacitance C . Due to the series connection of the two junctions within the SQUID loop, we obtain a total capacitance of $C/2$. The SQUID with its loop inductance L_s will therefore form an LC resonator that can be excited if the Josephson currents oscillate with the resonance frequency $f_{L_s C} = \frac{1}{2\pi\sqrt{L_s C/2}}$. This is fulfilled for the condition

$$\frac{V_s}{\Phi_0} = \frac{1}{2\pi\sqrt{L_s C/2}} \quad , \quad (1.44)$$

where V_s denotes the voltage drop across the SQUID that is associated with the Josephson frequency $f_J = \frac{V_s}{\Phi_0}$ resulting from the ac Josephson effect. With optimal β_C and β_L values the voltage corresponding to this resonance frequency will move towards the vicinity of the working point, thus becoming relevant for the SQUID's performance. This so-called *fundamental SQUID resonance* negatively affects the operation range by manifesting itself through a current step in the IVC, as shown in figure 1.10. The IV curves for integer and half integer flux quanta intersect as a result multiple times, due to higher harmonics of the resonance causing additional current steps [Cla04]. The voltage swing ΔV and consequently V_Φ are therefore limited by this resonance, which favors the choice of small values for L_s and C .

It is important to note, that the fundamental resonance does not depend on any geometrical structures of the circuit, which typically play a significant role in practical SQUIDS. Resonance inducing structures are however necessary for practical reasons.

Those include the need for effectively coupling external flux changes into the SQUID in order to take advantage of its high sensitivity. For this an external input coil with inductance L_i is usually fabricated on top of the SQUID loop, separated by an insulating layer to ensure the coupling to be solely inductive (see section 2.1). The SQUID can therefore be used as a current sensor by converting small current signals in the input coil into small magnetic flux changes in the SQUID. This added coil, however, provides another parasitic capacitance C_p resulting from its fabrication on top of the SQUID loop. Consequently, rf currents can couple inductively from one system into the other, causing further parasitic effects. Particularly, problematic LC resonances arise from the added inductance L_i and capacitance C_p , namely the $f_{L_s C_p}$ and $f_{L_i C_p}$ resonance. The latter can be excited for $f_J = f_{L_i C_p}$, since the Josephson currents are able to couple into the input coil. The parasitic capacitance C_p and consequently both resonance frequencies depend on geometrical factors such as the length of the input coil, as well as the widths and heights of the individual components that form the resonator. It has been shown, that these resonances lead to the energy sensitivity increasing proportional to $\sqrt{1 + 2C_p/C}$, as long as $C_p/C \leq 2$. For $C_p/C \geq 2$ the energy sensitivity saturates due to the resonance frequencies falling below the working point [Ryh92]. It is therefore desirable to minimize C_p as much as possible in order to reduce the resulting voltage noise.

The fabrication of the input coil on top of the SQUID loop also represents a microstrip transmission line, consisting of a conductor carrying the signal (input coil) and a ground plane (SQUID loop), separated by a dielectric layer. This forms a waveguide allowing electromagnetic waves to propagate alongside it, which undergo reflections where impedance mismatches occur. These would arise whenever the input coil exits the SQUID loop, thereby leaving the underlying ground plane. Standing waves occur if the length l of the signal carrying line above the ground plane corresponds to an integer number of half the wavelength of the Josephson frequency. The corresponding resonance frequency

$$f_l = \frac{m c_{\text{str}}}{2l} \quad , \quad (1.45)$$

where $m \in \mathbb{Z}$, depends therefore on l and the wave propagation velocity c_{str} . This resonance behavior also emerges if we consider the SQUID loop to be the signal carrying line with the input coil acting as the corresponding ground plane. Here it is again possible to move the resonance further away from the operation frequency at the working point by choosing adequate geometric proportions, e.g. by varying the length of the input coil or the SQUID loop. These methods to mitigate the influence of resonances can be complemented by direct damping through attenuators, which will be discussed in section 2.5. The following chapter will cover how various pa-

rameters are chosen in the SQUID design to suppress and avoid possible resonances, given the constraints we derived in subsection 1.2.3 and 1.2.4.

2. Experimental Setup

So far we discussed general aspects of dc-SQUIDs and how their working principle allows for highly sensitive magnetic flux measurements. As already briefly seen in subsection 1.2.5, when it comes to practical SQUIDs many theoretical considerations regarding parameter optimization need to be reevaluated to account for usability in practical experiments. We begin this chapter with general concepts of a practical SQUID design and introduce a typical low-noise setup with a room temperature readout electronic. In this working group, SQUIDs are mainly developed for the readout of *Metallic Magnetic Calorimeters (MMCs)* (see section 2.3). We will see in the following how those SQUIDs need to be designed to optimize their coupling to these detectors. Furthermore, this chapter will cover various methods to reduce quality factors of parasitic resonances, such as adding shunt resistors or coupling to normal conducting gold layers.

2.1 Practical dc-SQUIDs

The SQUIDs developed in this working group are used as current sensors for the MMC readout by sending the detected signals from the *pickup coil* of the MMC to the input coil of the SQUID. The requirement of the latter entails a parasitic capacitance resulting in numerous resonances, as discussed in subsection 1.2.5. To achieve high inductive coupling between input coil and SQUID loop, it is necessary to fabricate them closely on top of each other, only separated by a thin insulating layer. The coupling strength is given by the dimensionless parameter

$$k_{\text{is}} = \frac{M_{\text{is}}}{\sqrt{L_{\text{i}}L_{\text{s}}}} \quad , \quad (2.1)$$

where $M_{\text{is}} = \Delta\Phi_{\text{s}}/\Delta I_{\text{i}}$ is the mutual inductance, describing how much flux $\Delta\Phi_{\text{s}}$ is generated in the SQUID loop for a current change ΔI_{i} in the input coil. This allows us to define the so-called coupled energy sensitivity $\epsilon_{\text{c}}(f)$ with respect to the input coil, which by using equation 1.38 is given as

$$\epsilon_{\text{c}}(f) = \frac{\epsilon(f)}{k_{\text{is}}^2} = \frac{L_{\text{i}}S_{I,\text{i}}}{2} \quad . \quad (2.2)$$

This expression refers to the apparent current noise $S_{I,\text{i}} = S_{\Phi_{\text{s}}}/M_{\text{is}}^2$, which is generated by the flux noise from the SQUID loop through the coupling M_{is} . A strong

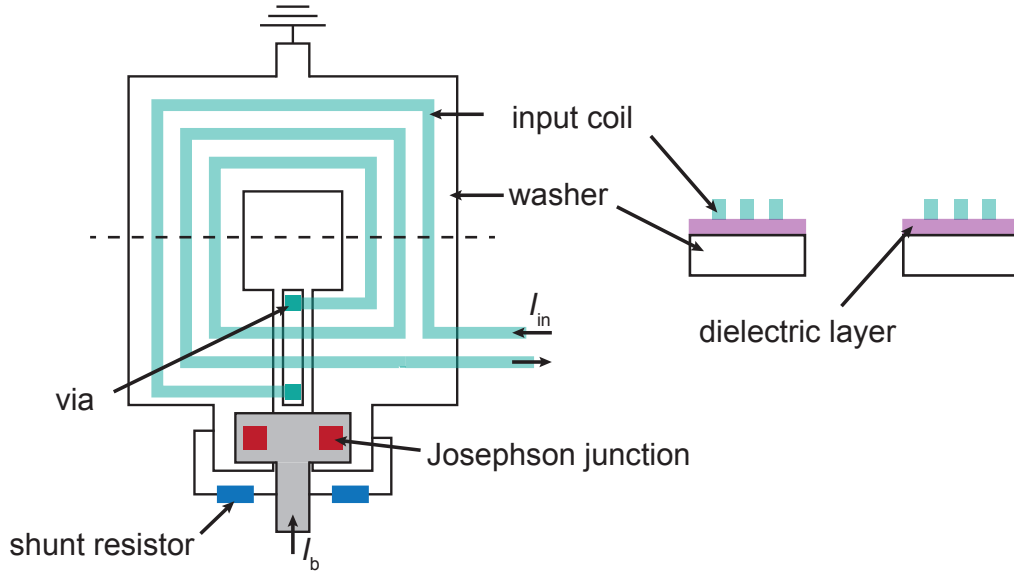


Figure 2.1: Schematic drawing of a typical planar thin-film dc-SQUID. The SQUID loop is realized as a square washer-geometry interrupted by a narrow slit, only connected at the junction area. A thin insulating layer separates the washer from the planar multi-turn input coil above. Left: View from the top. Right: Cross section marked by the dashed line.

coupling can be achieved by the commonly used square *washer*-geometry with a planar input coil [Jay81], as shown in figure 2.1.

Here, the SQUID loop is represented by the washer, whereas each turn of the input coil is symmetrically located on top of it to maximize the coupling between each system. A cross section of this setup is depicted in figure 2.1 (right), showing the insulating dielectric layer separating each coil. The washer is intersected by a slit, which starts at the square hole in the middle and ends at the remotely situated junction area that connects each side of the loop. The total inductance of the SQUID loop can be calculated by adding the dominating washer hole inductance L_h , the slit inductance $L_t \approx 0.3 \frac{\text{pH}}{\mu\text{m}}$ and the much smaller parasitic inductance L_j associated with the junction area, giving [Ket91]

$$L_s = L_h + L_t + L_j \quad . \quad (2.3)$$

The latter is referred to as parasitic due to its position outside of the input coil, thus not contributing to the coupling. By neglecting L_t and L_j , we can approximate the washer inductance in the limit of $d \ll w$ to $L_s \approx L_h \approx 1.25\mu_0 d$, where d and w are the inner and outer side lengths, respectively [Jay81]. This is a reasonable result considering that the supercurrent will only flow along the inner edge of the washer

[Ket82], thereby being independent of the outer side length w . The effective area A_{eff} of the SQUID loop has been calculated to $A_{\text{eff}} \approx dw$ [Ket85], showing that this geometry allows for high sensitivity while keeping the SQUID inductance small. The input coil inductance on the other hand can be approximated by $L_i = L_{\text{str}} + n^2 L_s$, where L_{str} is the stripline inductance (see section 2.5) and n is the number of input coil turns [Jay81]. The dc-SQUID designs used in this working group, however, are too complex to provide such analytical expressions and therefore need to be calculated numerically using simulation softwares such as *InductEX*.

2.1.1 Gradiometer

The high flux sensitivity of a SQUID makes it prone to detect unwanted magnetic bias fields and/or gradients that may be present during its operation. Typical SQUIDs are therefore built in a gradiometric design to counteract this effect [Ket78]. A first order gradiometer consists of two identical conducting loops connected in series or parallel, with opposing orientation as shown in figure 2.2 (left, middle). Under the presence of a homogeneous bias field \mathbf{B} in x-direction (perpendicular to the gradiometer plane), this configuration produces a zero net current after a field change ΔB_x , due to the opposing currents induced in each turn. To also achieve the same effect for a field gradient $\frac{\partial \mathbf{B}}{\partial z}$ or $\frac{\partial \mathbf{B}}{\partial y}$, a second order gradiometer composed of four loops in series or parallel is required, see figure 2.2 (right), where only the currents induced in the upper loops are drawn for the sake of overview. In order to incorporate this into a practical SQUID, the input coil and the SQUID loop will consist of four serial and parallel turns, respectively. This configuration enables to combine a small SQUID inductance with a large input coil inductance while maintaining a strong coupling between the two, as each turn of both coils can be produced with similar dimensions. The low SQUID inductance results from the reciprocal summation over each loop inductance L_w due to the parallel connection, giving

$$L_s = \frac{L_w}{4} . \quad (2.4)$$

Whereas a serial gradiometer gives

$$L_i = 4L_w \quad (2.5)$$

for the input coil. This gradiometric setup allows for adapting the input coil to the pickup coil of an MMC by choosing a large enough inductance L_i , which will be discussed in section 2.4.

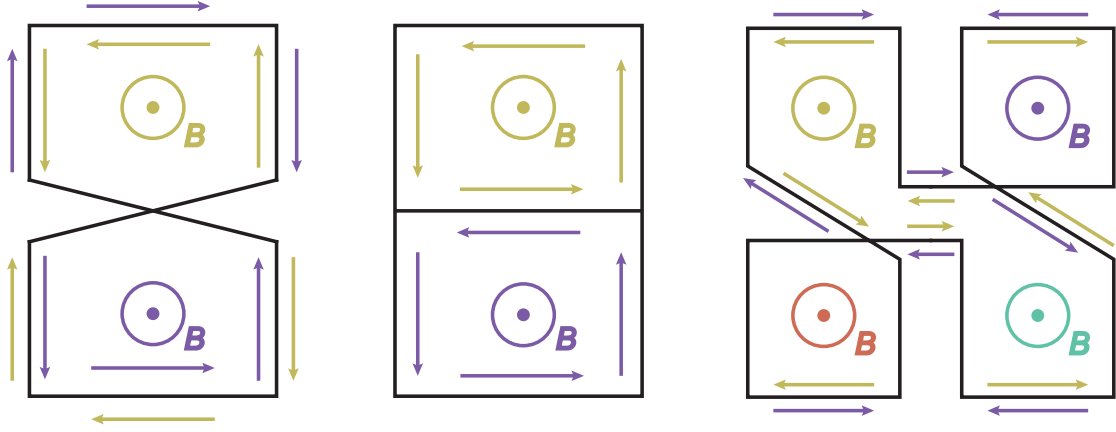


Figure 2.2: Schematic examples of a gradiometric dc-SQUID configuration threaded by a homogeneous magnetic field \mathbf{B} . A first order gradiometer can be realized by either connecting two loops in series (left) or in parallel (middle). A magnetic field change ΔB_x induces two opposing currents that cancel each other out. Right: Second order gradiometer consisting of four loops connected in series. This geometry results in a net zero current also for an applied field gradient $\frac{\partial \mathbf{B}}{\partial z}$.

2.2 Operation of a dc-SQUID

We have seen in section 1.2.2 that the periodic $V\Phi$ -characteristic provides an approximately linear dependency at $\Phi = (2n+1)\frac{\Phi_0}{4}$, which only holds for $\Delta\Phi \approx \Phi_0/4$. This restricts the dynamic range greatly, as the linearity vanishes for larger flux changes and for $\Delta\Phi > \Phi_0/2$ the voltage even becomes ambiguous. Such behavior is unsuitable for MMC readout, as they require the highest possible signal to noise ratio and therefore a linearized output voltage.

2.2.1 Flux-Locked Loop

The standard readout method involves a flux feedback circuit to maintain the operation at the working point independently of the flux change amplitude [Dru02]. This so-called flux-locked loop (FLL) readout technique first amplifies the output signal of the SQUID V_s with a differential amplifier operated at room temperature, where the voltage V_b corresponding to the working point is provided by a voltage source on the second amplifier input. This voltage compensation at the working point ensures that only variations $\Delta V = V_s - V_b$ that correspond to the flux change $\Delta\Phi$ are amplified. The signal is then fed into an integrator, which integrates it over time and thus creates a rising output voltage V_{out} . By now connecting a feedback resistance R_{fb} to

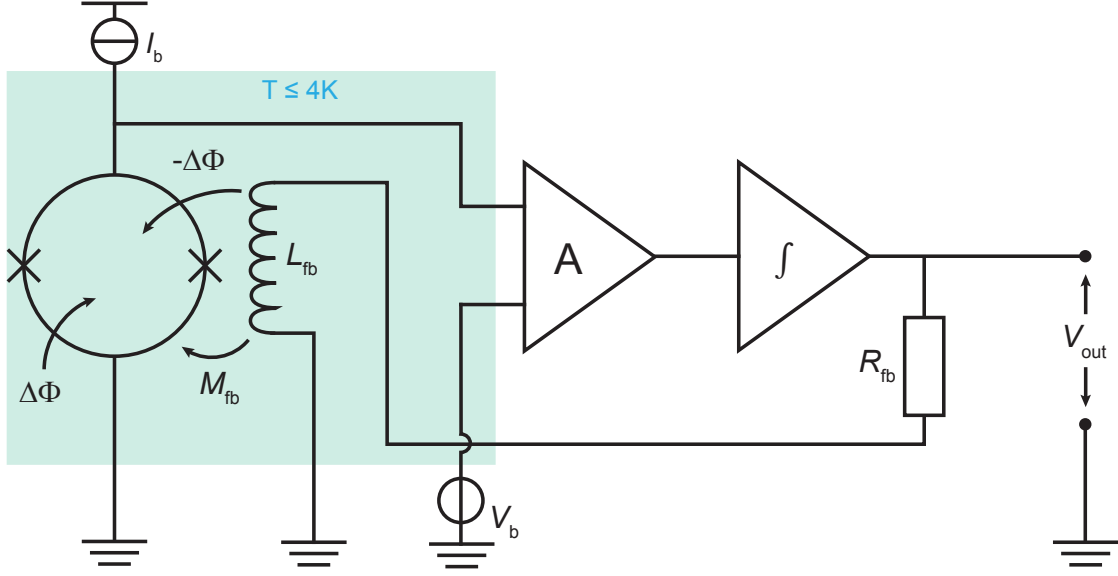


Figure 2.3: Schematic circuit diagram of a flux-locked loop dc-SQUID readout. The amplified and integrated SQUID voltage signal V_s , which is caused by a detected flux change $\Delta\Phi$, is fed back to a feedback coil with inductance L_{fb} , creating a compensating flux $-\Delta\Phi$. This enables the operation at the working point, while flux changes far greater than $\Phi_0/4$ can be linearized.

the output circuit, a rising feedback current I_{fb} emerges that flows to a feedback coil with inductance L_{fb} . This coil is coupled to the SQUID analogous to the input coil (see section 2.4), but with the opposite orientation. A compensation flux $-\Delta\Phi$ is generated up until the initial flux change is fully canceled out, i.e. $V_s \rightarrow 0$. The integrator will therefore approach a constant value due to the vanishing voltage at the input circuit. This voltage signal is proportional to the current that was needed to completely compensate for the input signal that induced $\Delta\Phi$, leading to the relation

$$V_{out} = \frac{R_{fb}}{M_{fb}} \Delta\Phi . \quad (2.6)$$

A schematic for this readout process is shown in figure 2.3. With this setup the SQUID is used as a null-detector that allows for the linearization of the quantity of interest, while also providing a large dynamic range. A state-of-the-art, low-noise SQUID readout electronic by the company Magnicon¹ of the type XXF-1, which is used in this working group, provides the necessary current and voltage sources, as well as the room temperature amplifiers within the FLL circuit described above.

¹Magnicon GmbH, Barkahusenweg 11, 22339 Hamburg

This SQUID electronic exhibits an intrinsic voltage noise of $\sqrt{S_{V,\text{el}}} \approx 0.33 \frac{\mu\text{V}}{\sqrt{\text{Hz}}}$ and intrinsic current noise of $\sqrt{S_{I,\text{el}}} \approx 2.6 \frac{\text{pA}}{\sqrt{\text{Hz}}}$ [Dru06]. Furthermore, a large amplifier bandwidth of 6 MHz is provided to ensure high sensitivity for short signal rise times. The intrinsic noise of the SQUIDs produced in this working group, however, typically reaches values of $\sqrt{S_{\Phi_s}} \leq 1 \frac{\mu\Phi_0}{\sqrt{\text{Hz}}}$. Adding these terms together leads to the total apparent flux noise in the SQUID, which is expressed as the spectral power density

$$S_{\Phi_s,\text{SQ}} = S_{\Phi_s} + \frac{S_{V,\text{el}}}{V_{\Phi_s}^2} + \frac{S_{I,\text{el}}}{I_{\Phi_s}^2} . \quad (2.7)$$

Typical values for the transfer coefficients of SQUIDs produced within the scope of this thesis, are $V_{\Phi_s} = 80 \frac{\mu\text{V}}{\Phi_0}$ and $I_{\Phi_s} = 20 \frac{\mu\text{A}}{\Phi_0}$, leading to the SQUID electronic having a total noise contribution of $4.13 \frac{\mu\Phi_0}{\sqrt{\text{Hz}}}$. The amplifier noise therefore dominates the noise level, thereby deteriorating the signal to noise ratio. To avoid this effect, a second SQUID is typically added to act as a low temperature amplifier [Wel93]. This method significantly reduces the apparent flux noise in the detector SQUID, which is crucial for MMC readout, as the intrinsic noise of a MMC detector should not be lower than that of the readout electronics.

2.2.2 Two-Stage Configuration

Implementing a low temperature amplifier is usually realized through a second stage SQUID, situated between the first stage (detector) SQUID and the room temperature amplifier, as depicted in figure 2.4. Here, the subscripts 's' and 'x' refer to the first and second stage, respectively. The first stage SQUID, also referred to as a Front-End SQUID, needs to be operated in a voltage bias for this two-stage setup. This can be achieved by connecting a gain resistor R_g in parallel with both the Front-End and the input coil of the amplifier SQUID. If a bias current $I_{b,s}$ is injected into the circuit, all the current will flow through the Front-End, as long as it stays superconducting. Once it becomes normal conducting by further increasing $I_{b,s}$, the current will start shifting to R_g , whose resistance is chosen to be much smaller than the dynamic resistance R_{dyn} , until most of the current flows through R_g . At this point, the resulting voltage across both components becomes approximately constant. This behavior can be visualized through a loadline created by the parallel resistances, which intersects the IVC of the Front-End. The loadline voltage V_s between both extremal IV curves will then remain nearly constant, as the slope is given by the small gain resistance R_g . If a detector signal is now coupled into the Front-End through the input coil with M_{is} , the current in the SQUID will move along the loadline in the $I\Phi$ -plane, corresponding to the externally induced flux Φ_s . The attached input coil of the second stage SQUID would experience these current changes, hence creating a

flux change $\Delta\Phi_x$ in the amplifier SQUID, which is being operated in a current bias. To maximize the amplification, the second stage SQUID is typically realized as a N -SQUID series array consisting of N serially connected identical SQUID cells. This results in a large voltage drop across the array, given by $V_{\text{array}} = NV_{\text{cell}}$. Analogous to the single stage readout, the signal will then be amplified at room temperature and fed back to a feedback coil with mutual inductance M_{fs} to compensate for the initial flux change $\Delta\Phi_s$. An additional feedback coil with mutual inductance M_{fx} , spanning symmetrically across every SQUID cell couples a constant flux offset through a bias current I_{Φ_x} into the array in order to maintain it at its working point. The resulting two-stage $V_x\Phi_s$ -characteristic will strongly depend on the flux gain defined as

$$G_\Phi = \frac{\partial\Phi_x}{\partial\Phi_s} = \frac{M_{\text{ix}}}{R_g + R_{\text{dyn}}} V_{\Phi_s} \approx \frac{M_{\text{ix}}}{R_{\text{dyn}}} V_{\Phi_s} \quad , \quad (2.8)$$

which relates the flux change induced in the second stage SQUID for a given flux change in the detector SQUID. For $\Delta\Phi_x = \Delta I_s M_{\text{ix}} > \Phi_0/2$, additional minima and maxima emerge. These start to overlap for $\Delta\Phi_x > \Phi_0$, thereby creating multiple working points that prevent a practical FLL operation. This sets an upper limit for the flux gain, however, it should be chosen as large as possible to reduce the apparent flux noise of the Front-End SQUID. An optimal flux gain has been calculated to $G_\Phi \approx \pi$, corresponding to $\Delta\Phi_x \approx \Phi_0/2$ [Dru96a].

The two-stage setup contributes additional noise sources to equation 2.7, namely the gain resistor and the amplifier SQUID. However, the resulting conversion to the flux Φ_s of the detector SQUID significantly reduces the influence of the room temperature amplifier, which in turn strongly improves the overall signal to noise ratio. The total apparent flux noise of the Front-End then reads [Dru96a]²

$$S_{\Phi_s, \text{SQ}} = S_{\Phi_s} + \frac{4k_B T R_g}{G_\Phi^2 (R_g + R_{\text{dyn}})^2} M_{\text{ia}}^2 + \frac{S_{\Phi_x}}{G_\Phi^2} + \frac{S_{\text{V,el}}}{G_\Phi^2 V_{\Phi_x}^2} + \frac{S_{\text{I,el}}}{G_\Phi^2 I_{\Phi_x}^2} \quad . \quad (2.9)$$

The second term describes the Nyquist current noise caused by the gain resistor, which becomes negligible with a voltage biased detector SQUID where $R_g \ll R_{\text{dyn}}$. The low and room temperature amplifier terms are reduced by the flux gain parameter, which can't be chosen arbitrarily large as mentioned above. However, using a SQUID array for the second stage increases the voltage swing and thus the transfer coefficient by an N -fold, i.e. $V_{\Phi_x} = NV_{\Phi_{\text{cell}}}$, where the subscript 'cell' refers to a single array SQUID cell. Consequently, the total noise level can be further reduced by choosing a high number N of SQUID cells. Here it is noteworthy, however, that

²Auch Stromquellen, siehe F. Kaap?

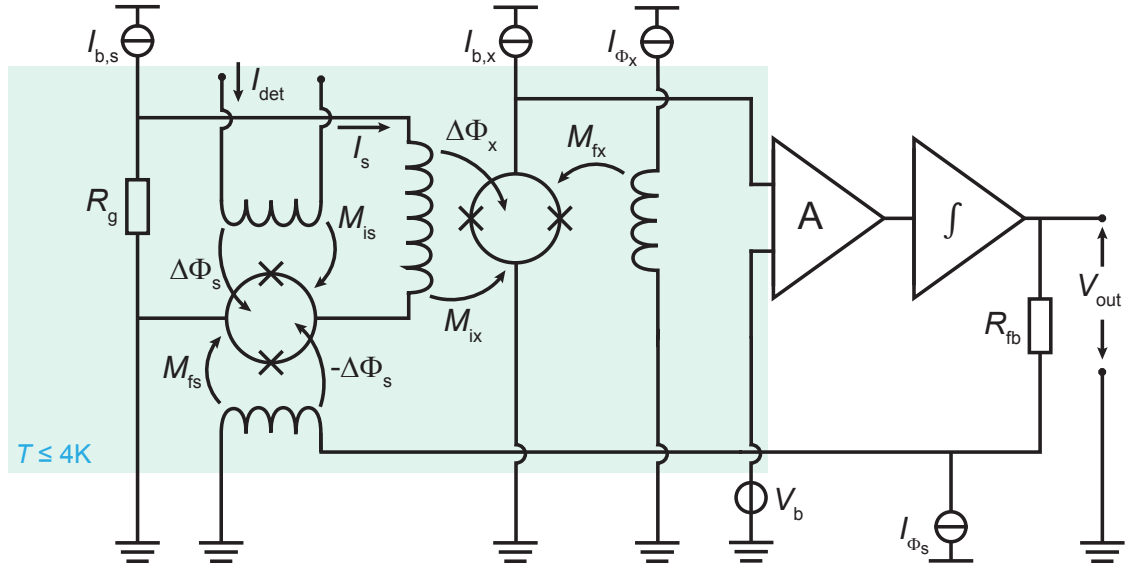


Figure 2.4: Schematic circuit diagram of a two-stage dc-SQUID based readout. The first stage consisting of the detector SQUID is voltage biased for $R_g \ll R_{dyn}$. The detector signal I_{det} induces a current change ΔI_s and therefore a flux change $\Delta\Phi_x$ in the second stage SQUID, which acts as a low temperature preamplifier. In FLL mode, the signal will be fed back to compensate for the initial flux change $\Delta\Phi_s$, thereby linearizing the detector signal. Choosing an N-SQUID series array amplifies the voltage swing and transfer coefficient, thus significantly reducing the overall apparent flux noise in the detector SQUID.

these considerations only account for the magnetic flux in a single cell, as otherwise the transfer coefficient would remain constant [Sta93],[Fog93]. Now, using equation 1.39 we obtain for the SQUID array flux noise

$$\sqrt{S_{\Phi_x}} = \frac{\sqrt{S_{V_x}}}{V_{\Phi_x}} = \frac{\sqrt{N S_{V_{cell}}}}{N V_{\Phi_{cell}}} = \frac{1}{\sqrt{N}} \sqrt{S_{\Phi_{cell}}} \quad , \quad (2.10)$$

hence the intrinsic noise of the second stage gets reduced by a factor of $\frac{1}{\sqrt{N}}$ [Sta93]. This also has a consequence for the coupled energy sensitivity of the SQUID array, which is calculated by summing the array flux noise over all N cells, giving

$$\epsilon_{c,x} = N \frac{S_{\Phi_x}}{2L_{cell}k_{i,cell}} = \frac{S_{\Phi_{cell}}}{2L_{cell}k_{i,cell}} \quad . \quad (2.11)$$

with the parameter $k_{i,cell}$ denoting the coupling of a cell with inductance L_{cell} to its respective input coil segment. Connecting N SQUIDs in series did therefore not affect the energy sensitivity, provided that $k_{i,cell}$ remains constant across the array. The

arrays produced in this working group either contain 16 [Kem15] or 18 [Kra23] cells. Applying this to equation 2.9, we would reduce the above-mentioned contribution of the room temperature amplifier flux noise of $4.13 \frac{\mu\Phi_0}{\sqrt{\text{Hz}}}$ to $0.29 \frac{\mu\Phi_0}{\sqrt{\text{Hz}}}$ and $0.26 \frac{\mu\Phi_0}{\sqrt{\text{Hz}}}$ for $N = 16$ and $N = 18$, respectively. Provided an optimal flux gain of $G \approx \pi$, the noise contribution would further decrease to $0.09 \frac{\mu\Phi_0}{\sqrt{\text{Hz}}}$ or $0.08 \frac{\mu\Phi_0}{\sqrt{\text{Hz}}}$, well below the typical noise level of a detector SQUID.

Besides the improvement of the noise behavior, a major advantage of a two-stage readout setup consists of the low power dissipation produced by the detector SQUID. As opposed to the current bias operation in a single-stage setup, the Front-End is held at a constant, low voltage, such that the dissipated power given by $P = UI$ only consists of approximately 1 nW [Dru07]. However, this amount poses a problematic heat source for low temperature detectors consisting of up to millions of temperature-sensitive calorimeter pixels, such that using a two-stage setup for each pixel is unfavorable. For these, a different approach using time- or frequency-division dc-SQUID multiplexing is followed. These readout techniques constitute a research focus in this working group in order to optimize the readout of several experiments such as the ECHo experiment [Gas17].

2.3 Metallic Magnetic Calorimeters

Low temperature detectors used in this working group exhibit detector arrays consisting of MMC pixels, which are able to absorb and detect heavy particles or photons such as X-rays. The focus of this thesis was to improve the dc-SQUID based MMC readout, which is why we first briefly cover the working principle of such calorimeters.

A general overview of the detector setup can be seen in figure 2.5. The upper part consists of a particle absorber, which, following the law of energy conservation, converts the energy E of an incoming particle into a change in temperature ΔT in the absorber. A paramagnetic sensor is directly attached below, submerged in a weak magnetic field. Strong thermal coupling allows for an effective temperature increase in the sensor, which is given by the total heat capacity C_{tot} of both the sensor and the absorber, resulting in

$$\Delta T \simeq \frac{E}{C_{\text{tot}}} . \quad (2.12)$$

Not shown in figure 2.5 is an underlying thermal bath weakly linked to the sensor, which reverts the temperature change by an exponential decay ensures a thermal equilibrium. The paramagnetic nature of the sensor changes its magnetization $M(T)$

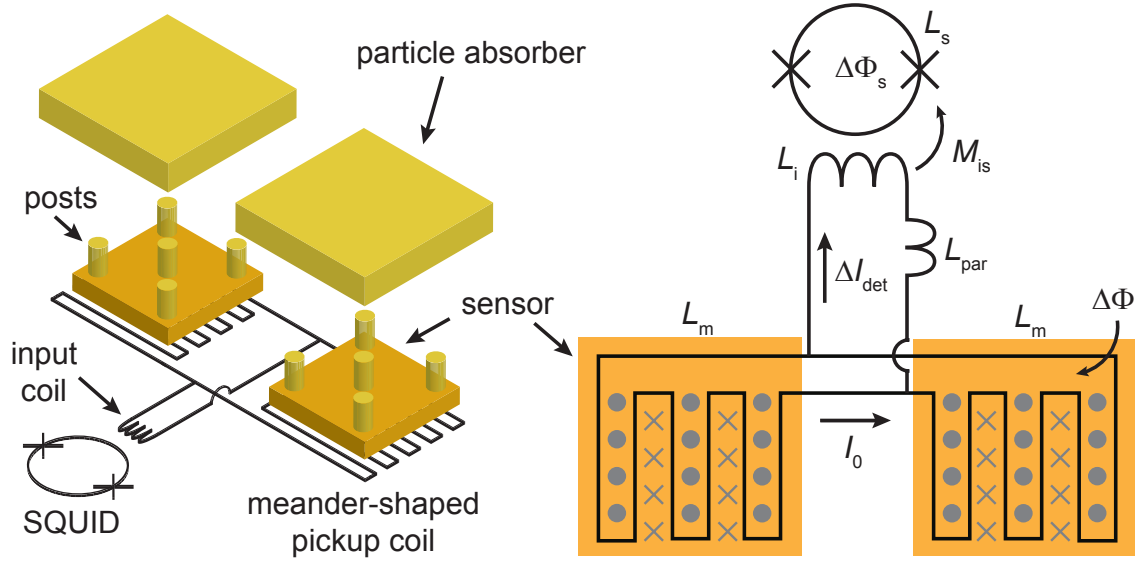


Figure 2.5: Schematic depiction (left) and circuit diagram (right) of a common MMC channel consisting of two pixels. The planar particle absorber is fabricated on top of the paramagnetic sensor, separated by cylinder-shaped posts to prevent energy losses through athermal phonons, while still providing good thermal coupling. Below the sensors two meander-shaped pickup coils connected in parallel detect the flux change $\Delta\Phi$, which can be precisely measured with a SQUID as a flux transformer. The grey dots and crosses within the meander mark a magnetic field induced by the bias current I_0 .

upon a temperature rise, according to the Curie law $M \propto \frac{1}{T}$ for low temperatures. This induces a magnetic flux change $\Delta\Phi$ linear proportional to ΔM , which is detected by a typically meander-shaped pickup coil that is strongly coupled to the sensor. The input coil of the SQUID is directly connected to the pickup coil forming a flux transformer, thereby enabling the readout of the created current signal ΔI_{det} . With equation 2.12 we can write for the induced flux in the SQUID

$$\Delta\Phi_s \propto \Delta\Phi \propto \Delta M \simeq \frac{\partial M}{\partial T} \frac{E}{C_{\text{tot}}} \quad , \quad (2.13)$$

provided the deposited energy E is small. Evidently, it is desirable to both reduce the heat capacity and increase the magnetization gradient in order to maximize the flux change $\Delta\Phi$. Additionally, short signal rise times can be realized by a high thermal conductivity of the sensor and the absorber, which is particularly crucial for coincidence measurements. All these material-dependent requirements are fulfilled for the normal conducting metal gold as an absorber material and gold or silver for the sensor. The latter needs to be doped with a few hundred ppm of the rare-earth

metal erbium in order to obtain paramagnetic properties. State-of-the-art MMCs of this kind were successfully developed in this working group, providing an exceptional energy resolution, a large energy bandwidth and fast signal rise times well below 100 ns [Kem18].

The detector geometry shown in figure 2.5 is widely used in this working group. Two meander-shaped pickup coils, each with an inductance L_m , are connected as a parallel gradiometer and are located beneath their respective sensor pixel, with a connection to the input coil of the flux transformer. As the SQUID is typically placed far away to mitigate the influence of its heat dissipation, a parasitic inductance L_{par} needs to be taken into account due to the wiring between the SQUID and the detector (figure 2.5, right). A constant small bias current I_0 is injected into the pickup coils to provide the weak bias field needed for the paramagnet. If now a particle gets detected by one of the absorbers, a flux change $\Delta\Phi$ and thus a current is induced in the meander. By applying Kirchhoffs first law and knowing that magnetic flux in a closed superconducting loop is conserved [Lan60], we can calculate the resulting current signal in the input coil to [Bur04]

$$\Delta I_{\text{det}} = \frac{\Delta\Phi}{L_m + 2(L_i + L_{\text{par}})} \quad . \quad (2.14)$$

A significant advantage of this setup lies in the fact, that only one SQUID is needed to readout two pixels. The gradiometer geometry ensures, that depending on which absorber gets hit, the current ΔI_{det} will flow in one direction or the other. Thus, every pixel can be assigned a polarity of the resulting flux in the SQUID loop, making them distinguishable. Together with the mutual inductance $M_{\text{is}} = \frac{\Delta\Phi}{\Delta I_{\text{det}}}$ between the input coil and the SQUID loop, we can now introduce the flux-to-flux coupling

$$\frac{\Delta\Phi_s}{\Delta\Phi} = \frac{M_{\text{is}}}{L_m + 2(L_i + L_{\text{par}})} \quad , \quad (2.15)$$

which is maximal for $L_i = \frac{L_m}{2} + L_{\text{par}}$. This crucial parameter is a measure for the flux gain and gives therefore information about the quality of the readout setup. Consequently, it is desirable to choose the optimal input coil inductance L_i for a given pickup coil inductance $L_p = \frac{L_m}{2}$.

2.3.1 Extrinsic Energy Sensitivity

In this regard it is reasonable to discuss one aspect of the noise behavior for this readout setup. Just like the flux change originating in the detector induces a flux change in the SQUID, it is also possible to happen the other way around. The

intrinsic flux noise of the SQUID can therefore also couple into the pickup coil, creating the apparent flux noise $\sqrt{S_{\Phi_s, p}}$ in the detector. To quantify this noise influence, we define analogous to equation 1.38 the extrinsic energy sensitivity with respect to a given pickup coil inductance L_p as [Knu88]

$$\epsilon_p = \frac{S_{\Phi_s, p}}{2L_p} \quad (2.16)$$

Here, it is necessary to point out that the choice of a single coil with inductance L_p adds a factor of 2 to equations 2.14 and 2.15, such that the flux-to-flux coupling reads

$$\frac{\Delta\Phi_s}{\Delta\Phi_p} = \frac{M_{is}}{L_p + L_i + L_{par}} \quad (2.17)$$

This advantage, however, does not outweigh the above-mentioned benefit to readout two pixels with one read-out electronic, as the gradiometric design also cancels out unwanted signals through changes in external magnetic field or substrate temperature [Man21]. In the following we consider the case for a single pickup coil with inductance $L_p = \frac{L_m}{2}$. The presence of a flux transformer is accompanied with a shielding effect with respect to the SQUID loop, such that the geometric inductance is reduced to an effective inductance given by [Gro16]

$$L'_s = L_s(1 - k_{is}^2 s_{in}) \quad (2.18)$$

where $s_{in} = \frac{L_i}{L_i + L_p + L_{par}}$ denotes the screening factor [Cla04], which reaches the value of 0.5 for the condition $L_i = L_p + L_{par}$ that minimizes the flux-to-flux coupling. By now using the relation $\frac{\Delta\Phi_s}{\Delta\Phi_p} = \frac{\sqrt{S_{\Phi_s}}}{\sqrt{S_{\Phi_s, p}}}$, we finally obtain with equation 2.16 to 2.18 the extrinsic energy sensitivity [Knu88]

$$\epsilon_p = \frac{S_{\Phi_s}(L_i + L_{par} + L_p)^2}{2L_p M_{is}^2} = \frac{S_{\Phi_s}(L_i + L_{par} + L_m/2)}{L_s k_{is}^2 s_{in} L_m / 2} \quad (2.19)$$

This parameter is minimized by maximizing the flux-to-flux transfer $\frac{\Delta\Phi_s}{\Delta\Phi_p}$ as well as minimizing the intrinsic flux noise of the SQUID S_{Φ_s} given by the expressions derived in subsection 1.2.4. Finding the minimum for the latter provides optimal values for the shunt resistors R_s and the SQUID loop inductance L_s , as we will see in the following section.

2.4 dc-SQUID Design

The main objective for this thesis was the optimization of an existing Front-End SQUID design for an improved coupling to one of the detectors being developed in this working group. As we have seen in the previous section 2.3, adjusting L_i to the detector coil ensures the maximization of the flux-to-flux coupling and therefore minimizes the extrinsic energy sensitivity. The previous SQUID design exhibits an input coil inductance of $L_i = 1.64$ [Bau22], which is well suited for the pickup coil inductance of the ECHO-100k detector of $L_p = 1.14$ nH [Man21]. The parasitic inductance L_{par} arises from the aluminum bonds between the SQUID and the detector substrate to form the flux transformer and has been estimated to 0.5 nH [Hen17]. Other MMC detectors from this working group such as the 4k-pixel molecule camera MOCCA and the X-ray detector maXs100 require higher input inductances, as their pickup coil inductances are $L_p = 8.8$ nH and $L_p = 6.65$ nH, respectively. In [Bau22] SQUIDs with matching input inductances for the MOCCA and maXs100 detector were developed for the first time using an intermediary coupling transformer. These improved the energy resolution ΔE_{FWHM} of the detectors, although the effect was minimal for the latter due to a reduction of the effective coupling constant k'_{is} , compensating the gain through an increased input inductance of $L'_i = 5.47$ nH. A new approach was followed in the framework of this thesis

2.4.1 dc-SQUID with a Two-Turn Input Coil

Figure: Front-End with Li=6 (klayout and microscope?)

Explain all the design details including design parameters like L_s , L_i , R_s , R_d .

Also explain how we don't expect flux vortices to play an important role for the washer width of 10 μm .

Talk about the value of $\frac{\Delta\Phi_s}{\Delta\Phi_p}$ that we would expect given the design values. The same for ϵ_p .

2.4.2 Integrated Two-Stage Chip

Figure: Int. 2stage chip (klayout and microscope?)

Briefly cover its features

2.5 Damping Methods

Talk about how resistors are used to damp resonances, like R_d and $R_x C_x$.

Figure: Comparison of two IVC plots, one with $R_x C_x$, one without (see Fabienne Diss.) (?)

Figure: Schematic circuit diagram of our SQUIDs with all L's, C's and R's

2.5.1 Lossy Input Coil

Figure: FE with lossy layer highlighted (klayout and microscope?)

Explain briefly why it could help, citing the only paper we found for this specific application so far

2.5.2 Inductive Damping

Figure: Feedlines with goldpads on top.

I have not found any info about this method in papers or other publications.. I have only a handwavy explanation in mind on how it should work.

3. Experimental Results

3.1 Characteristic dc-SQUID Parameters

Discuss various measured/simulated parameters such as $R_s, R_n, \Delta V, I_c, \beta, L_s, L_i, M$'s and calculate $\frac{\Delta\Phi_s}{\Delta\Phi_p}, \epsilon_p$. Summarize the values in a table. Compare with previous FEs and literature.

3.1.1 Input Coil Inductance

Explain the method to measure L_i , compare the result with expected value.

3.2 Resonance Behavior

Discuss in more detail all types of resonances with formulae and calculate the frequencies (there are still two of them that are unclear/need to be discussed in private or in a meeting)

Figures: All measured FE IVCs, like non-lossy, lossy, damping variants, iso, no-iso, no input coil, Fabiennes FE... (should I also show the corresponding VPhi curves?)

Try to identify the resonances in the plots. Discuss what actually helped damping and what not.

3.3 Noise Performance

3.3.1 Lumped Element Two-Stage Setup

Figures: Show noise measurements at mK (3 setups from SQUID Cryo, 1 setup from Mocca Cryo)

Discuss all contributions, especially from the FE -> Difference if input coil is shorted or not?

Are 2stage VPhi curves interesting or do we restrict ourselves to noise plots?

3.3.2 Integrated Two-Stage Setup

Figure: Int. 2stage noise measurement

Summarize Fabians measurements and compare with ours.

4. Summary

Bibliography

- [Bar57] J. Bardeen, L. N. Cooper, and J. R. Schrieffer, Theory of Superconductivity, *Phys. Rev.*, **108**(5), 1175–1204, 1957.
- [Bau22] Fabienne Bauer, *Rauscharme Stromsensor-dc-SQUIDs mit Impedanzanpassung für metallische magnetische Kalorimeter*, Dissertation, Kirchhoff-Institut für Physik, Universität Heidelberg, 2022.
- [Bru82] J. J. P. Bruines, V. J. de Waal, and J. E. Mooij, Comment on: “DC SQUID: Noise and optimization” by Tesche and Clarke, *J. Low Temp. Phys.*, **46**, 383–386, 1982.
- [Bur04] Andreas Burck, *Entwicklung großflächiger magnetischer Kalorimeter zur energieaufgelösten Detektion von Röntgenquanten und hochenergetischen Teilchen*, Diplomarbeit, Kirchhoff-Institut für Physik, Universität Heidelberg, 2004.
- [Cla88] J. Clarke and R. Koch, The Impact of High Temperature Superconductivity on SQUIDs, *Science*, **242**, 217–223, 1988.
- [Cla04] J. Clarke and A. I. Braginski (Ed.), *The SQUID Handbook: Vol. 1, Fundamentals and Technology of SQUIDs and SQUID Systems*, Wiley-VCH, 2004.
- [Dea61] B. S. Deaver and W. M. Fairbank, Experimental Evidence for Quantized Flux in Superconducting Cylinders, *Phys. Rev. Lett.*, **7**, 43–46, 1961.
- [Dru96a] D. Drung, Advanced SQUID read-out electronics, in H. Weinstock (Ed.), *SQUID sensors: Fundamentals, Fabrication and Application*, NATO ASI Series E329. Dordrecht: Kluwer, 1996.
- [Dru96b] D. Drung, F. Ludwig, W. Müller, U. Steinhoff, L. Trahms, H. Koch, Y. Q. Shen, M. B. Jensen, P. Vase, T. Holst, T. Freltoft, and G. Curio, Integrated $\text{YBa}_2\text{Cu}_3\text{O}_{7-x}$ magnetometer for biomagnetic measurements, *Appl. Phys. Lett.*, **68**, 1421–1423, 1996.
- [Dru02] D. Drung, High-performance DC SQUID read-out electronics, *Physica C: Superconductivity*, **368**(1-4), 134–140, 2002.

-
- [Dru06] D. Drung, C. Hinnrichs, and H.-J. Barthelmess, Low-noise ultra-high-speed dc SQUID readout electronics, *Supercond. Sci. Tech.*, **19**(5), S235, 2006.
 - [Dru07] D. Drung, C. Abmann, J. Beyer, A. Kirste, M. Peters, F. Ruede, and Th. Schurig, Highly sensitive and easy-to-use squid sensors, *IEEE Transactions on Applied Superconductivity*, **17**(2), 699–704, 2007.
 - [Dru11] D. Drung, J. Beyer, J.-H. Storm, M. Peters, and T. Schurig, Investigation of Low-Frequency Excess Flux Noise in DC SQUIDS at mK Temperatures, *IEEE T. Appl. Supercon.*, **21**, 340–344, 2011.
 - [Fog93] V. Foglietti, K.G. Stawiasz, M.B. Ketchen, and R.H. Koch, Performance of a flux locked series SQUID array, *IEEE T. Appl. Supercon.*, **3**(4), 3061–3065, 1993.
 - [Gas17] L. Gastaldo, K. Blaum, K. Chrysalidis, T. Day Goodacre, A. Domula, M. Door, H. Dorrer, Ch. E. Düllmann, K. Eberhardt, S. Eliseev, C. Enss, A. Faessler, P. Filianin, A. Fleischmann, D. Fonnesu, L. Gamer, R. Haas, C. Hassel, D. Hengstler, J. Jochum, K. Johnston, U. Kebschull, S. Kempf, T. Kieck, U. Köster, S. Lahiri, M. Maiti, F. Mantegazzini, B. Marsh, P. Neroutsos, Yu. N. Novikov, P. C. O. Ranitzsch, S. Rothe, A. Rischka, A. Saenz, O. Sander, F. Schneider, S. Scholl, R. X. Schüssler, Ch. Schweiger, F. Simkovic, T. Stora, Z. Szücs, A. Türlér, M. Veinhard, M. Weber, M. Wegner, K. Wendt, and K. Zuber, The electron capture in 163ho experiment – ECHo, *The European Physical Journal Special Topics*, **226**(8), 1623–1694, 2017.
 - [Gin50] V. L. Ginzburg and L. Landau, On the theory of superconductivity, *Zh. Èksper. Teoret. Fiz.*, **20**, 1064–1082, 1950.
 - [Gro16] R. Gross, A. Marx, and F. Deppe, *Applied Superconductivity: Josephson Effect and Superconducting Electronics*, De Gruyter Textbook Series, Walter De Gruyter Incorporated, 2016.
 - [Hen17] Daniel Hengstler, *Development and characterization of two-dimensional metallic magnetic calorimeter arrays for the high-resolution X-ray spectroscopy*, Dissertation, Kirchhoff-Institut für Physik, Universität Heidelberg, 2017.
 - [Ina80] Akira Inaba, Superconductive transition point of tantalum and niobium as a reference temperature, *Japanese Journal of Applied Physics*, **19**(8), 1553, 1980.

-
- [Iva68] Yu. M. Ivanchenko and L. A. Zil'berman, Destruction of Josephson Current by Fluctuations, *ZhETF*, **8**, 113–115, 1968.
- [Jay81] J. M. Jaycox and M. B. Ketchen, Planar coupling scheme for ultra low noise dc SQUIDs, *IEEE Transactions on Magnetics*, **17**(1), 400–403, 1981.
- [Jos62] B. D. Josephson, Possible new effects in superconductive tunnelling, *Physics Letters*, **1**(7), 251–253, 1962.
- [Jos65] B. D. Josephson, Supercurrents through barriers, *Advances in Physics*, **14**(56), 419–451, 1965.
- [Kem15] S. Kempf, A. Ferring, A. Fleischmann, and C. Enss, Direct-current superconducting quantum interference devices for the readout of metallic magnetic calorimeters, *Superconductor Science and Technology*, **28**(4), 45008, 2015.
- [Kem18] S. Kempf, A. Fleischmann, L. Gastaldo, and C. Enss, Physics and Applications of Metallic Magnetic Calorimeters, *Journal of Low Temperature Physics*, 1–15, 2018.
- [Ket78] M. B. Ketchen, W. M. Goubau, J. Clarke, and G. B. Donaldson, Superconducting thinfilm gradiometer, *J. Appl. Phys.*, **49**, 4111–4116, 1978.
- [Ket82] M. B. Ketchen and J. M. Jaycox, Ultra-low-noise tunnel junction dc SQUID with a tightly coupled planar input coil, *Applied Physics Letters*, **40**(8), 736–738, 1982.
- [Ket85] A. W. Kleinsasser et al. Ketchen, W. J. Gallagher, Dc squid flux focuser, in H. D. Hahlbohm und H. Lübbig (Ed.) (Ed.), *SQUID'85 Superconducting Quantum Interference Devices and their Applications: Proceedings of the Third International Conference on Superconducting Quantum Devices, Berlin (West), June 25-28, 1985*, 865–871, Walter de Gruyter, 1985.
- [Ket91] M.B. Ketchen, Design considerations for DC SQUIDs fabricated in deep sub-micron technology, *IEEE T. Magn.*, **27**, 2916–2919, 1991.
- [Knu88] J. Knuutila, M. Kajola, H. Seppä, R. Mutikainen, and J. Salmi, Design, Optimization, and Construction of a DC SQUID with Complete Flux Transformer Circuits, *Journal of Low Temperature Physics*, **71**(5-6), 369–392, 1988.
- [Koc07] Roger H. Koch, David P. DiVincenzo, and John Clarke, Model for $1/f$ flux noise in squids and qubits, *Phys. Rev. Lett.*, **98**, 267003, 2007.

- [Kra23] F. Kraemer, *Development and characterization of an integrated two-stage dc-SQUID for the read-out of metallic magnetic calorimeters*, Bachelor thesis, Kirchhoff-Institut für Physik, Universität Heidelberg, 2023.
- [Lan60] L.D. Landau, L.P. Bell, E.M. Lifshitz, and J.B. Sykes, *Electrodynamics of Continuous Media*, Volumen 8 in *Course of Theoretical Physics*, Ney York: Pergamon Press, 1960.
- [Lik86] K. K. Likharev, *Dynamics of Josephson Junctions and Circuits*, Gordon and Breach, New York, 1986.
- [Man21] Federica Mantegazzini, *Development and characterisation of high-resolution metallic magnetic calorimeter arrays for the ECHo neutrino mass experiment*, Dissertation, Kirchhoff-Institut für Physik, Universität Heidelberg, 2021.
- [McC68] D. E. McCumber, Effect of ac Impedance on dc Voltage-Current Characteristics of Superconductor Weak-Link Junctions, *Journal of Applied Physics*, **39**(7), 3113–3118, 1968.
- [Mei33] W. Meissner and R. Ochsenfeld, Ein neuer Effekt bei Eintritt der Supraleitfähigkeit, *Naturwissenschaften*, **21**(44), 787–788, 1933.
- [Ryh92] Tapani Ryhänen, Heikki Seppä, and Robin Cantor, Effect of parasitic capacitance and inductance on the dynamics and noise of dc superconducting quantum interference devices, *Journal of Applied Physics*, **71**(12), 6150–6166, 1992.
- [Sta93] K. G. Stawiasz and M. B. Ketchen, Noise Measurements of Series SQUID Arrays, *IEEE T. Appl. Supercon.*, **3**, 1808–1811, 1993.
- [Ste68] W. C. Stewart, Current-Voltage Characteristics of Josephson Junctions, *Applied Physics Letters*, **12**(8), 277–280, 1968.
- [Tes77] C. D. Tesche and J. Clarke, dc SQUID: Noise and Optimization, *Journal of Low Temperature Physics*, **294**(3), 1–9, 1977.
- [Tie21] Eite Tiesinga, Peter J. Mohr, David B. Newell, and Barry N. Taylor, Co-data recommended values of the fundamental physical constants: 2018, *Rev. Mod. Phys.*, **93**, 025010, 2021.
- [Wel93] R.P. Welty and J.M. Martinis, Two-stage integrated squid amplifier with series array output, *IEEE Transactions on Applied Superconductivity*, **3**(1), 2605–2608, 1993.